

## Substituent effects on dynamics at conical intersections: Allene and methyl allenes

Simon P. Neville,<sup>1</sup> Yanmei Wang,<sup>2</sup> Andrey E. Boguslavskiy,<sup>1,3,4</sup> Albert Stolow,<sup>1,3,4,a)</sup> and Michael S. Schuurman<sup>1,3,b)</sup>

<sup>1</sup>Department of Chemistry, University of Ottawa, 10 Marie Curie, Ottawa, Ontario K1N 6N5, Canada

<sup>2</sup>State Key Laboratory of Magnetic Resonance and Atomic and Molecular Physics, Wuhan Institute of Physics and Mathematics, Chinese Academy of Sciences, Wuhan 430071, People's Republic of China

<sup>3</sup>National Research Council of Canada, 100 Sussex Drive, Ottawa, Ontario K1A 0R6, Canada

<sup>4</sup>Department of Physics, University of Ottawa, 150 Louis Pasteur, Ottawa ON K1N 6N5, Canada

(Received 5 October 2015; accepted 10 December 2015; published online 6 January 2016)

We report a joint experimental and theoretical study on the ultrafast excited state dynamics of allene and a series of its methylated analogues (1,2-butadiene, 1,1-dimethylallene, and tetramethylallene) in order to elucidate the conical intersection mediated dynamics that give rise to ultrafast relaxation to the ground electronic state. We use femtosecond time-resolved photoelectron spectroscopy (TRPES) to probe the coupled electronic-vibrational dynamics following UV excitation at 200 nm (6.2 eV). *Ab initio* multiple spawning (AIMS) simulations are employed to determine the mechanistic details of two competing dynamical pathways to the ground electronic state. In all molecules, these pathways are found to involve as follows: (i) twisting about the central allenic C–C–C axis followed by pyramidalization at one of the terminal carbon atoms and (ii) bending of allene moiety. Importantly, the AIMS trajectory data were used for *ab initio* simulations of the TRPES, permitting direct comparison with experiment. For each molecule, the decay of the TRPES signal is characterized by short (30 fs, 52 fs, 23 fs) and long (1.8 ps, 3.5 ps, [306 fs, 18 ps]) time constants for 1,2-butadiene, 1,1-dimethylallene, and tetramethylallene, respectively. However, AIMS simulations show that these time constants are only loosely related to the evolution of electronic character and actually more closely correlate to large amplitude motions on the electronic excited state, modulating the instantaneous vertical ionization potentials. Furthermore, the fully substituted tetramethylallene is observed to undergo qualitatively different dynamics, as displacements involving the relatively massive methyl groups impede direct access to the conical intersections which give rise to the ultrafast relaxation dynamics observed in the other species. These results show that the branching between the “twisting” and “bending” pathways can be modified via the selective methylation of the terminal carbon atoms of allene. The interplay between inertial and potential effects is a key to understanding these dynamical branching pathways. The good agreement between the simulated and measured TRPES confers additional confidence to the dynamical picture presented here. © 2016 AIP Publishing LLC. [<http://dx.doi.org/10.1063/1.4938561>]

### I. INTRODUCTION

The excited state non-adiabatic dynamics of polyatomic molecules generally involves dynamics at conical intersections (CIs). Specific vibrational motions at or near conical intersections play a key role in determining electronic branching and, therefore, the outcomes of photochemical processes. The use of methyl substitution as a means to alter excited state vibrational motions, thereby influencing the conical intersection mediated dynamics, has been studied previously in a series of unsaturated hydrocarbons.<sup>1–7</sup> Here, we study the molecule allene and a series of its methylated analogues.

The photochemistry of allene and the elucidation of its photodissociation, in particular, have been an ongoing focus of study for decades.<sup>8</sup> That this molecule has sustained such

a level of interest stems from its importance as a prototypical polyene and the large number of dissociation pathways which are energetically accessible following UV excitation. A principal focus of these studies was the comparison of the photodissociation products (and energy distributions) between allene and other structural isomers, most notably 1-propyne.<sup>9–12</sup> A consensus was established which states that both molecules first undergo internal conversion to the ground electronic state and then isomerize, ultimately dissociating in the “hot” ground electronic state. The evidence for this picture is that the product yields and kinetic energy distributions are indistinguishable for these two species.<sup>10,12</sup>

The excited state dynamics resulting in electronic relaxation to the ground state were inferred from *ab initio* electronic structure computations.<sup>13,14</sup> In particular, these predict intersections between the ground and first excited electronic states when there is a twist about the C–C–C axis and/or angle bend about this axis, as well as the coordinates resulting in H<sub>2</sub> loss.<sup>13</sup> *Ab initio* computed barriers

<sup>a)</sup>Electronic address: [albert.stolow@nrc-cnrc.gc.ca](mailto:albert.stolow@nrc-cnrc.gc.ca)

<sup>b)</sup>Electronic address: [michael.schuurman@nrc-cnrc.gc.ca](mailto:michael.schuurman@nrc-cnrc.gc.ca)

to dissociation suggest that photoexcitation around 193 nm (6.4 eV) is followed by internal conversion to the ground electronic state before fragmentation, in broad agreement with experimental results.

Upon methylation of one of the terminal carbon atoms (yielding 1,2-butadiene), the predicted photodissociation processes are qualitatively similar: UV excitation is followed by internal conversion to the ground state which then has sufficient energy to dissociate along one of the number of accessible channels. When photoexcited at 193 nm, the primary dissociation pathways are  $\text{CH}_3$  and H-atom loss,<sup>15–17</sup> although more fragmentation products are observed as one moves to higher excitation energies.<sup>18,19</sup> In a recent time-resolved study on the dynamics leading to photodissociation, employing a two-photon 400 nm pump followed by a 42 nm probe photon generated via high-harmonic generation (HHG), an excited state lifetime of  $37 \pm 15$  fs was determined.<sup>20</sup> As part of the same study, trajectory simulations on the  $S_1$  electronic surface only (non-adiabatic transitions between states were not considered) found population localizing near a conical intersection geometry corresponding to a twist of the terminal  $\text{CH}_2$  group about the C–C–C axis.

The goals of the present work are twofold. First, we aim to definitively ascertain the mechanistic details of the internal conversion process in allene. Second, the selective methylation of the terminal carbon atoms of allene is systematically explored in order to study inertial and density of state effects on dynamics at conical intersections and as a potential route to control excited state non-adiabatic dynamics. To do so, we combined time-resolved photoelectron spectroscopy (TRPES)<sup>21–23</sup> experiments with *ab initio* trajectory simulations on allene and a series of its methylated analogues: 1,2-butadiene (1,2-BD), 1,1-dimethylallene (DMA), and tetramethylallene (TMA). The substitution of heavier methyl groups for light H atoms influences the nature of the conical intersection mediated non-adiabatic dynamics and provides an illuminating basis for comparison of the dynamics in this analogous series.<sup>2,3</sup> Trajectory simulations on allene and its methyl substituted analogues were carried out to both uncover mechanistic pathways and to determine the effects of methylation on the non-adiabatic dynamics. Importantly, in order to unambiguously compare experiment with theory, *ab initio* simulations of the experimental TRPES, based on the trajectory simulations, were carried out and compared directly to the experimental results.

The outline of this paper is as follows: in Sections II and III, we summarize the experimental and theoretical methods employed; in Section IV, we present the results of this study; in Section V, we articulate the vibronic mechanism for the excited state dynamics that emerges from the computational and spectroscopic results; and in Section V, we summarize the key conclusions of this study.

## II. EXPERIMENTAL METHODS

Our femtosecond time-resolved magnetic bottle photoelectron spectroscopy method was previously described in detail in Ref. 24. The measurements were carried out with  $\lambda_{\text{pump}} = 200$  nm (6.20 eV) and  $\lambda_{\text{probe}} = 266.7$  nm (4.65 eV).

Pulsed seeded supersonic molecular beams containing 1,2-butadiene (Organic technologies, 98%), 1,1-dimethylallene (Aldrich,  $\geq 97\%$ ), or tetramethylallene (Aldrich,  $\geq 97\%$ ) were introduced to the interaction region via a 1 kHz pulsed supersonic valve (Even-Lavie, 150  $\mu\text{m}$  diameter aperture nozzle) using helium carrier gas at a stagnation pressure of  $\sim 4$  bars. These samples were used without further purification. In the seeded molecular beam, the samples were pre-mixed with helium at concentrations of 4.8% (1,2-BD), 1.5% (DMA), and 0.22% (TMA).

Femtosecond laser pulses centered at 800 nm with 1 kHz repetition rate were obtained from a Ti:sapphire regenerative amplifier, followed by a single pass amplifier stage (Coherent Legend Elite Duo). Approximately 500  $\mu\text{J}$  of the output was used for harmonic generation to produce 200 nm and 267 nm laser pulses, based on sum-frequency mixing in thin BBO crystals. Vacuum ultraviolet-grade calcium fluoride prism pairs were used to compress the generated UV pulses and to pre-compensate for dispersion along the beam paths. The UV pulse durations were measured directly with an autocorrelator based on two-photon absorption.<sup>25</sup> Typical autocorrelation traces, along with pulse spectra measured with a UV spectrometer (Ocean Optics Maya Pro), are shown in Figure S1 of the supplementary material.<sup>26</sup>

The pump-probe time delay was computer-controlled via a high-precision linear translation stage (Newport XML210). The beams were recombined collinearly on a dichroic mirror and softly focused using an  $f = 500$  mm spherical reflective mirror to intersect the seeded, pulsed molecular beam in the interaction region of a magnetic bottle photoelectron spectrometer. Photoelectron spectra from the pump or probe laser pulses were independently recorded and dynamically subtracted in order to correct for small background photoelectron signals generated from single laser multiphoton ionization. Pulse energies of  $\sim 140$  nJ at 200 nm and  $\sim 1.6$   $\mu\text{J}$  at 267 nm were used.

The *in situ* time zero overlap and cross-correlation between the pump and the probe pulses were determined by  $[1 + 1']$  photoionization of nitric oxide, which also served for electron kinetic energy calibration using the well-characterized two-photon ionization of NO.<sup>27,28</sup> The cross-correlation data are included in Table I.

## III. THEORETICAL METHODS

### A. *Ab initio* multiple spawning (AIMS)

We consider a system composed of  $f$  nuclear degrees of freedom  $R_\alpha$  and  $N_{el}$  electronic degree of freedom  $r_i$ . In the

TABLE I. Time constants from 2D global fitting of TRPES data for 1,2-BD, DMA, and TMA.

	IP (eV) <sup>a</sup>	Cross-correlation (fs)	$\tau_1$ (fs)	$\tau_2$	$\tau_3$ (ps)
1,2-BD	9.33	$63 \pm 5$	30	1.8 ps	
DMA	8.95	$68 \pm 5$	52	3.5 ps	
TMA	8.47	$68 \pm 5$	32	306 fs	18

<sup>a</sup>Vertical ionization potential value from Ref. 43.

AIMS method, the *ansatz* for the total molecular wavefunction  $|\Psi(\mathbf{R}, \mathbf{r}, t)\rangle$  reads

$$|\Psi(\mathbf{R}, \mathbf{r}, t)\rangle = \sum_{I=1}^{n_s} |\chi^I(\mathbf{R}, t)\rangle |I(\mathbf{r}; \mathbf{R})\rangle. \quad (1)$$

Here,  $|I\rangle$  denotes the  $I$ th electronic state, and  $|\chi^I\rangle$  the nuclear wavefunction associated with the  $I$ th electronic state. The electronic basis  $\{|I\rangle\}$  is chosen to correspond to the set of  $n_s$  lowest-lying adiabatic electronic states. Each nuclear wavefunction  $|\chi^I\rangle$  is expanded in terms of a set of  $f$ -dimensional frozen-width Heller-type Gaussian basis functions  $\{g_j^I\}$ ,

$$|\chi^I(\mathbf{R}, t)\rangle = \sum_{j=1}^{N_I} C_j^I(t) g_j^I(\mathbf{R}, t; \alpha_j^I, \bar{\mathbf{R}}_j^I(t), \bar{\mathbf{P}}_j^I(t), \gamma_j^I(t)), \quad (2)$$

where  $\alpha_j^I$ ,  $\bar{\mathbf{R}}_j^I(t)$ , and  $\bar{\mathbf{P}}_j^I(t)$  denote, respectively,  $f$ -dimensional vectors of Gaussian widths, positions, and momenta associated with each Cartesian coordinate  $R_\alpha$ . The positions and momenta,  $\bar{\mathbf{R}}_j^I(t)$  and  $\bar{\mathbf{P}}_j^I(t)$ , are taken to evolve according to classical equations of motion, whilst the phases  $\gamma_j^I(t)$  are propagated semi-classically. The equations of motion for the expansion coefficients  $C_j^I(t)$  are derived by insertion of wavefunction *ansatz* (1) and (2) into the time-dependent Schrödinger equation.

The set of Gaussian basis functions  $\{g_j^I\}$  is adaptively increased during the course of an AIMS calculation in a process referred to as spawning, so as to be able to describe internal conversion between electronic states. Briefly, when a given Gaussian basis function  $g_j^I$  enters region of strong non-adiabatic coupling between the electronic states  $|I\rangle$  and  $|J\rangle$ , additional basis functions  $g_j^J$  are created on the  $J$ th electronic state.<sup>29</sup>

## B. Calculation of time-resolved photoelectron spectra

We consider ionization from a manifold of  $N$ -electron states  $|I\rangle$  to a manifold of  $(N-1)$ -electron states  $|\alpha\rangle$ . In order to simulate the time-resolved photoelectron spectrum for a given system, we approximate the total photoelectron signal  $\sigma(E, t)$  at a given time to correspond to the incoherent sum of contributions from the relative probabilities of ionization  $W_{I\alpha}$  evaluated at the centres  $\bar{\mathbf{R}}_j^I$  of each Gaussian basis function in the corresponding AIMS calculation,<sup>30–35</sup>

$$\sigma(E, t) = \sum_{I=1}^{n_s^0} \sum_{\alpha=1}^{n_s^+} \sum_{j=1}^{N_I} |C_j^I(t)|^2 \times W_{I\alpha}(\bar{\mathbf{R}}_j^I(t)) \delta\left(E - \left(\omega - \Delta E_I^\alpha(\bar{\mathbf{R}}_j^I(t))\right)\right). \quad (3)$$

Here,  $\omega$  is the photon energy of the laser pulse,  $\Delta E_I^\alpha$  is the vertical energy difference between  $|I\rangle$  and  $|\alpha\rangle$ , and  $n_s^0$  and  $n_s^+$  denote the number of neutral and cationic electronic states, respectively. The  $\delta$ -function arises as we assume vertical ionization to occur. Previous studies<sup>36</sup> have shown that for the case of weak field ionization, the squares of the norms of the Dyson orbital  $\phi_{I\alpha}^D$ ,

$$\phi_{I\alpha}^D = \sqrt{N} \langle I|\alpha\rangle, \quad (4)$$

are good estimates of the relative probabilities of ionization  $W_{I\alpha}$ , and it is this approach that is taken in this work. A more detailed exposition of this approach is given in the supplementary material.

The calculated spectrum is broadened via convolution in the time domain using a Gaussian function with a full width at half maximum (FWHM) corresponding to the experimental cross-correlation between the pump and probe laser pulses. Furthermore, in order to account for both the finite widths of the Gaussian basis functions used in the AIMS calculations and the inherent resolution of the experimental spectrum, the calculated spectrum is convoluted in the energy domain using a Gaussian function with a FWHM  $\zeta \approx O(10^{-1})$  eV.

## C. Projected mode frequency analysis

We are interested in effects which govern the branching pathways between two different conical intersections. We expect that methylation may introduce both inertial (i.e. kinetic) and potential (i.e. electronic and steric) effects. The relative time scale for nuclear motion along two different internal coordinates  $s_k$ —in a given electronic state  $|I\rangle$  starting from a nuclear geometry  $\mathbf{R}$ —will be majorly influenced by two principal factors: (i) the difference in the curvatures of the potential  $V_I$  of the state  $|I\rangle$  with respect to the two coordinates and (ii) the masses of the atoms being displaced. To obtain a suitable metric for the relative time scale of nuclear motion along a given internal coordinate  $s_k$  that accounts for these two factors, we consider the calculation of a quantity which we term a projected mode (imaginary) frequency,  $\omega_{s_k}^I$ , obtained from a projection of the mass-weighted Hessian onto an infinitesimal displacement along the internal coordinate  $s_k$ ,

$$\omega_{s_k}^I(\mathbf{R}) = \{\tilde{\mathbf{s}}_k^T \mathbf{H}^I(\mathbf{R}) \tilde{\mathbf{s}}_k\}^{\frac{1}{2}}. \quad (5)$$

Here,  $\tilde{\mathbf{s}}_k$  denotes the normalized Cartesian displacement vector pointing in the direction of an infinitesimal displacement along the internal coordinate  $s_k$ , and  $\mathbf{H}^I(\mathbf{R})$  denotes the mass-weighted Hessian for the  $I$ th electronic state. In particular, we consider the ratio

$${}^I\Gamma_{s_j}^{s_k}(\mathbf{R}) = \frac{\omega_{s_k}^I(\mathbf{R})}{\omega_{s_j}^I(\mathbf{R})} \quad (6)$$

as a measure of the relative time scale for initial motions along the internal coordinates  $s_k$  and  $s_j$ . For  ${}^I\Gamma_{s_j}^{s_k}(\mathbf{R}) > 1$ , the time scale for initial motion along  $s_k$  may be expected to be shorter than that for displacement along  $s_j$ , whereas for  ${}^I\Gamma_{s_j}^{s_k}(\mathbf{R}) < 1$ , the opposite may be expected to hold. In our analysis, we only consider projected mode frequencies  $\omega_{s_k}^I(\mathbf{R})$  at the Franck-Condon (FC) point in the  $S_1$  state, and so drop both the state index  $I$  and the geometry dependence from  ${}^I\Gamma_{s_j}^{s_k}(\mathbf{R})$ , the context in which the symbol  $\Gamma_{s_j}^{s_k}$  is used for preventing any ambiguity.

## D. Computational details

In the AIMS simulations of the excited state dynamics of allene, 1,2-BD, DMA, and TMA, the requisite adiabatic energies, energy gradients, and non-adiabatic coupling terms

were evaluated at the multi-reference first-order configuration interaction (MR-FOCI) level. The underlying reference functions were taken as complete active space self-consistent field (CASSCF) wavefunctions employing an active space consisting of the two highest occupied  $\pi$  orbitals and the two lowest-lying unoccupied  $\pi^*$  orbitals, that is, four electrons in four orbitals. We denote this level of calculation by MR-FOCI(4,4). For allene, 1,2-BD, and DMA, the 6-31G\*\* basis was used for all calculations. Owing to the larger size of the TMA, the smaller 6-31G basis set was used for this system. All electronic structure calculations were performed using the COLUMBUS suite of programs.<sup>37</sup> The AIMS calculations were performed using the FMS90 program.

All AIMS calculations employed the manifold of electronic states spanned by the  $S_0$ ,  $S_1(\pi\pi^*)$ , and  $S_2(\pi\pi^*)$  states. The initial states corresponded to vertical excitation from the ground state to the  $S_1(\pi\pi^*)$  state, with the initial positions and momenta being sampled using a Monte Carlo procedure from the ground state Wigner distribution. To do so, the harmonic approximation was employed, with the required frequencies and normal modes calculated at the B3LYP/TZVP level using the Turbomole set of programs.<sup>38</sup> Propagation times of 300 fs were used, with time steps of 10 a.u. A total of 39 initial basis functions were used, with each being propagated independently, under the so-called independent first generation approximation.<sup>29</sup> To reduce computational costs, and acknowledging that our interests lie in the excited state dynamics of the systems under consideration, all basis functions spawned in the ground electronic state were removed from the propagations once their coupling to the other basis functions fell below a preset threshold value.

Owing to the limited accuracy of the computationally tractable MR-FOCI(4,4) calculations used in the AIMS calculations, the vertical ionization energies  $E_I^\alpha$  used in the calculation of the TRPES are not of sufficiently accurate to be used in their “raw” form. Instead, these terms are shifted by a constant amount  $\Delta E_I^\alpha$  determined such that the shifted values are brought into agreement with the vertical ionization energies calculated at a higher level of theory at the FC point. Specifically, the shifts  $\Delta E_I^\alpha$  were calculated at the equation-of-motion coupled-cluster with single and double excitations (EOM-CCSD) level using the aug-cc-pVDZ basis. All EOM-CCSD calculations were performed using the CFOUR program.<sup>39</sup> An additional positive shift of 0.35 eV was applied to the vertical ionization energies of TMA in order to bring the low energy parts of the calculated and experimental TRPES into agreement. This small empirical shift is justified as its magnitude is of the order of the expected accuracy of the vertical energy differences furnished by the EOM-CCSD method.

## IV. RESULTS

### A. Time-resolved photoelectron spectroscopy

The TRPES spectra of 1,2-BD, DMA, and TMA, pumped at 200 nm and probed at 267 nm, are shown in Figure 1. For each molecule, the decay associated spectra (DAS) extracted from two-dimensional global fits are shown beneath the

corresponding TRPES data. The total energy of one pump plus one probe photon [ $1 + 1'$ ] is 10.85 eV, whereas probing with two photons [ $1 + 2'$ ] yields 15.50 eV.

For 1,2-BD, the ionic ground state  $D_0$  can be reached by [ $1 + 1'$ ] ionization, yielding a photoelectron with a maximum kinetic energy of  $\sim 1.5$  eV. This energy agrees well with the cutoff of the intense maximum seen at low kinetic energies in the TRPES (Figure 1). Although the  $D_1$  cationic state could be reached by [ $1 + 1'$ ] ionization with an excess energy of  $\sim 0.8$  eV, we did not see any evidence of this channel in the TRPES data shown in Figure 1. The ionization channel accessed via [ $1 + 2'$ ] multiphoton ionization can be seen as the signal which cuts off at around 6.17 eV, as expected based on the IP. In order to determine time constants and their DAS, a 2D global least-squares method - explained in detail previously<sup>2,4</sup> - was employed to fit all photoelectron kinetic energies and time delays simultaneously using a standard Levenberg-Marquardt algorithm. In brief, the time- and energy-resolved photoelectron signal  $S(E, \Delta t)$  is described via a kinetic model through

$$S(E, \Delta t) = \sum_i A_i(E) P_i(\Delta t) \otimes g(\Delta t), \quad (7)$$

where  $A_i(E)$  is the time-independent, energy-resolved DAS of the photoionization channel associated with the  $i$ th time constant. The DAS  $A_i(E)$  has its overall amplitude, but not its shape, evolved in time by the function  $P_i(t)$  determined by the kinetic model and  $g(t)$  is the Gaussian cross-correlation function determined experimentally ( $\sim 67$  fs). We see a delayed onset to the rise of the photoelectron signals both for [ $1 + 1'$ ] and [ $1 + 2'$ ] ionizations, best seen in the spectrum normalized by energy slices shown in Figure 2. In cases where the TRPES spectrum shows a delayed onset, or “chirp,” towards lower kinetic energies at longer time delays, we interpret this as evidence of large amplitude motions which “sweep” the Franck-Condon spectrum of the ionizing transition towards lower kinetic energies. As discussed previously,<sup>4,5,22</sup> 2D global fitting schemes may not account easily for large amplitude motions which would require a time-dependent form for the DAS. A phenomenological method which accounts for this shift within 2D global fitting is to artificially permit the “time zero” to be a variable.<sup>5,40</sup> With such an approach, the variation in “time zero” can be associated with the “sweep” of the Franck-Condon spectrum due to large amplitude motions.

The time constants obtained from global fitting are presented in Table I. Two time constants were derived from the fit for 1,2-BD,  $\tau_1 = 30$  fs and  $\tau_2 = 1.8$  ps, respectively. From their DAS, both components have their origins at the [ $1 + 1'$ ] cutoff at 1.5 eV, with positive amplitude, indicating the decay of population from the initially excited  $\pi\pi^*$  state.

For DMA, similar results are observed. As shown in Figure 1, the  $D_0$  state is reached by [ $1 + 1'$ ] and [ $1 + 2'$ ] ionization schemes with excess energies of 1.90 eV and 6.55 eV, respectively. Two time constants of  $\tau_1 = 52$  fs and  $\tau_2 = 3.5$  ps emerged from the global fitting. The DAS associated with  $\tau_1$  is centered around 0.5 eV, whereas the DAS of  $\tau_2$  is centered near 0.2 eV. Both extend from 0 to  $\sim 2$  eV (near the cutoff of 1.90 eV in  $1 + 1'$  process) and each has positive amplitude components, indicating two independent

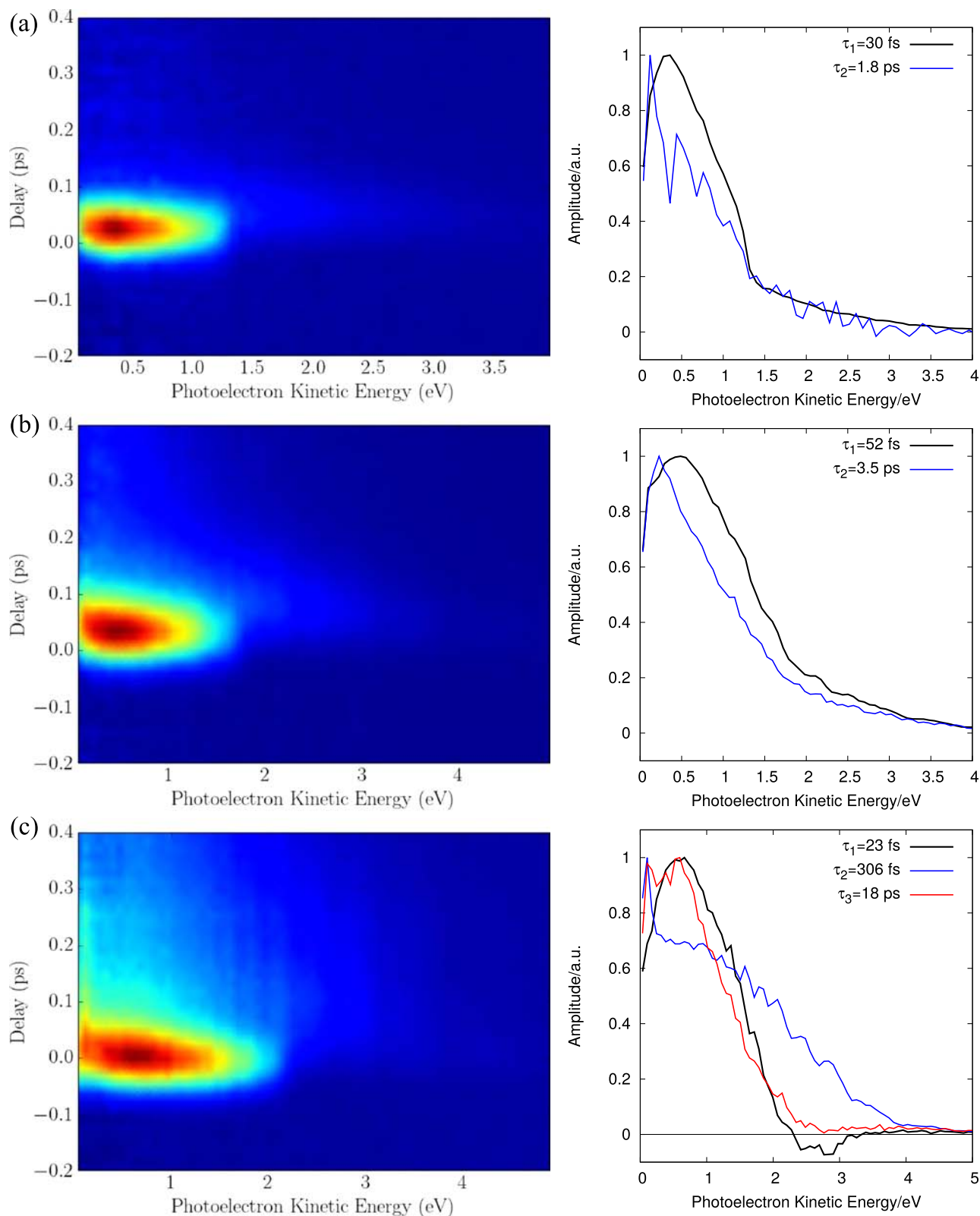


FIG. 1. Experimental TRPES spectra (left-hand column) and decay associated spectra (right-hand column) of (a) 1,2-BD, (b) DMA, and (c) TMA at pump and probe wavelengths of 200 nm and 267 nm, respectively.

decay channels from the initially populated state. We note that both lifetimes are longer than the corresponding ones in 1,2-butadiene. The “sweep” of the “time zero” in the DMA spectrum in Figure 2(b) is more obvious than that of 1,2-BD in Figure 2(a).

The energetic cutoffs for TMA are calculated to be around 2.38 eV for  $[1 + 1']$  ionization and 7.03 eV for  $[1 + 2']$  ionization. As shown in Figure 2(c), the normalized TRPES spectrum shift is the clearest amongst these three molecules. We find that three non-trivial (as determined by the reduced  $\chi^2$ )

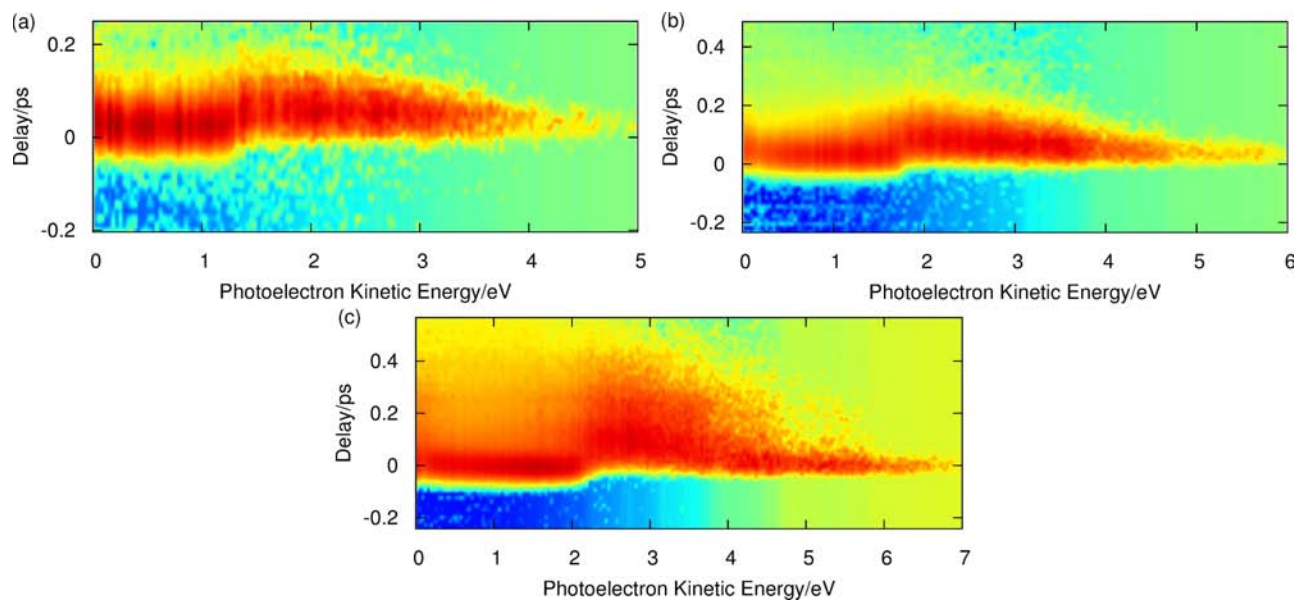


FIG. 2. TRPES spectra with independently normalized energy slices for (a) 1,2-BD, (b) DMA, and (c) TMA.

time constants are needed in the global fit. The first time constant,  $\tau_1 = 23$  fs, is very fast. The DAS associated with  $\tau_1$  has broad features ranging from 0 to  $\sim 2.3$  eV with all positive amplitude components, indicating a decay of population on a time scale  $\tau_1$ . Interestingly, in TMA, new weak but broad features ranging from 2.3 to 3.3 eV with negative amplitude components are observed. Beyond that is a long tail in the TRPES which has positive amplitudes up to  $\sim 7$  eV. The spectra associated with  $\tau_2$  and  $\tau_3$  each have broad features ranging from 0 to 4 eV and from 0 to 2.5 eV, respectively. The  $\tau_3$  lifetime is much longer than either  $\tau_1$  or  $\tau_2$ . Importantly, we note that oscillations are observed in the TRPES of TMA at low photoelectron kinetic energies. Shown in Figure 3 are the photoelectron intensities at an energy of 0.22 eV, which for time delays greater than 100 fs clearly show oscillations with an average period of 50 fs. This period corresponds

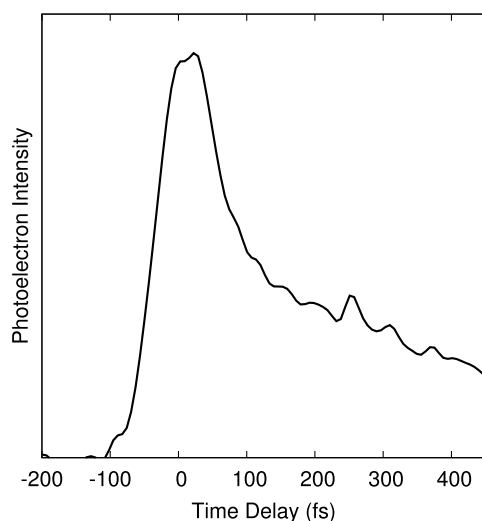


FIG. 3. Cut along the experimental TRPES of TMA at a photoelectron kinetic energy of 0.22 eV. Oscillations in the photoelectron intensity with a period of  $\sim 50$  fs can clearly be seen for time delays greater than 100 fs.

roughly to a  $670\text{ cm}^{-1}$  vibrational frequency. This oscillation appears at very low electron kinetic energy and persists for long times, conceivably resulting from photoionization of the vibrationally hot ground electronic state. However, as discussed in Section V, we argue that this coherent feature most likely results from large amplitude motion along the allenic C–C–C bending coordinate following the trapping of population in a low-energy bottleneck on the  $S_1$  potential energy surface.

## B. Potential energy surfaces (PESs)

We here discuss features common to the  $S_1$  potential energy surfaces of allene, 1,2-BD, DMA, and TMA which will prove relevant to the discussion of their excited state dynamics. We first consider the dihedral angle  $\psi$ , a twisting coordinate corresponding to the angle between the planes defined by the terminal C–X bonds and the allenic C–C–C unit, where  $X = \text{H}, \text{CH}_3$ . The definition of this angle for the case of allene is shown in Figure 4, with the definitions for 1,2-BD, DMA, and TMA following analogously. Shown in Figure 5 are the PESs for the  $S_0$  and  $S_1$  states of allene along the twisting coordinate  $\psi$ , as calculated at the MR-FOCI(4,4) level. The corresponding PESs for 1,2-BD, DMA, and TMA are all very similar and, therefore, for the sake of brevity, are not

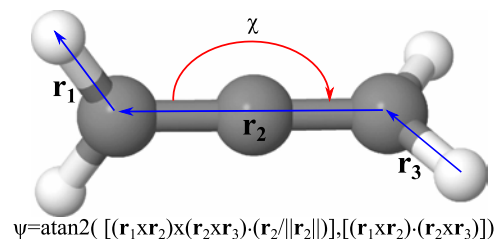


FIG. 4. Definition of the dihedral angle  $\psi$  and the bending angle  $\chi$  for the case of allene.

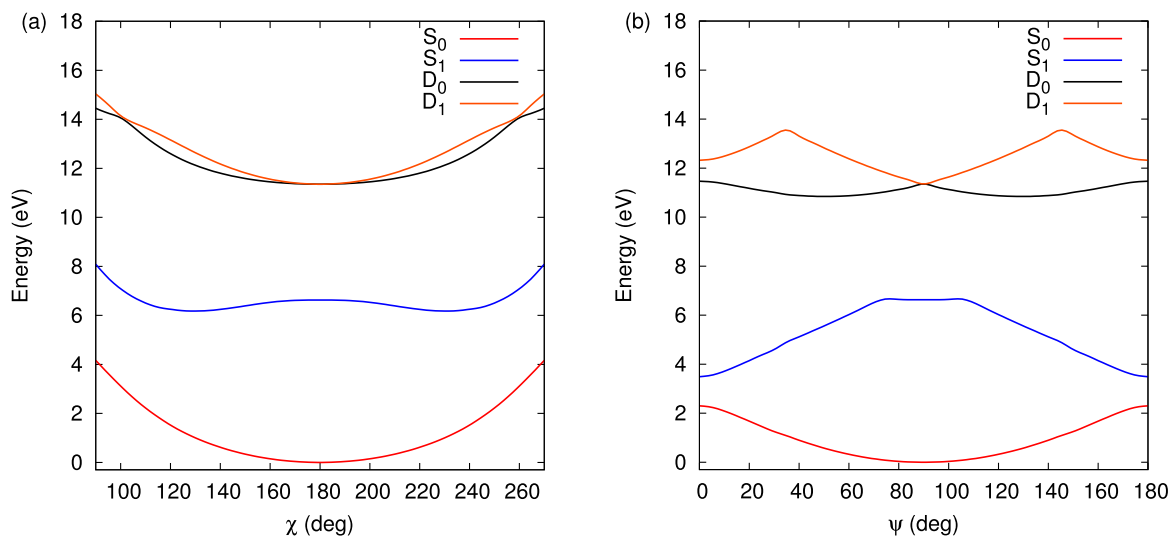


FIG. 5. Potential energy surface cuts for the  $S_0$ ,  $S_1$ ,  $D_0$ , and  $D_1$  states of allene along (a) the C–C–C bending coordinate  $\chi$  and (b) the dihedral angle  $\psi$ . Both cuts start from the Franck-Condon point ( $\chi = 180^\circ$ ,  $\psi = 90^\circ$ ) and correspond to unrelaxed calculations, that is, without the optimization of the degrees of freedom orthogonal to the one being displaced.

reproduced here. In all cases, the  $S_1$  potential possesses a local minimum at  $\psi = 0$ , corresponding to a quasi-planar nuclear configuration. Importantly, these local minima are considerably lower in energy than the FC point and are accessible via almost barrierless pathways from the Frank-Condon region. Furthermore, motion along these paths significantly reduces the energy gap between the  $S_0$  and  $S_1$  states. This “downhill” situation favours the projection mode analysis approach to dynamical branching, discussed above.

Second, the bending angle  $\chi$ , defined as the angle between the two vectors connecting the middle and end carbon atoms of the C–C–C backbone, is of interest. The  $S_0$  and  $S_1$  PESs for allene along the bending angle  $\chi$  are shown in Figure 5, with the corresponding PESs for 1,2-BD, DMA, and TMA being once again qualitatively similar. The  $S_1$  PESs of all three molecules are found to be at a maximum at the FC point with respect to the bending angle  $\chi$ . As will be discussed in detail in Section IV D 4, large amplitude motion along the bending degree of freedom is found to be of importance following excitation to the  $S_1$  state.

### C. Conical intersections

Optimizations of conical intersections between the  $S_0$  and  $S_1$  states were performed at the MR-FOCI(4,4) level for all four molecules, starting from the local minima present along each of the nuclear degrees of freedom  $\psi$  and  $\chi$ . The resulting minimum energy intersection geometries for allene are shown in Figures 6(a) and 6(b). For the sake of brevity, the minimum energy intersection geometries for the other molecules are given in Figure S2 of the supplementary material.<sup>26</sup> For allene, 1,2-BD, and DMA, two low-lying conical intersection geometries were found for each molecule. Significant similarities exist between the conical intersection geometries for each molecule and we consider them to belong to one of two distinct classes, “twisting” and “bending,” each being defined by the arrangement of the carbon atoms of the allenic C–C–C axis. The first

class (“twisting”), whose members we term the “Tw-Py” geometries, corresponds to rotation about the dihedral angle  $\psi$  followed by pyramidalization of the terminal  $\text{CH}_2$  units. The second class (“bending”), whose members we term the “Tw-B” geometries, corresponds to rotation about the dihedral angle  $\psi$  followed by bending of the C–C–C backbone. For TMA, no points of conical intersection were found. However, a point of near degeneracy ( $\Delta E \sim 0.05$  eV) between the  $S_0$  and  $S_1$  states was found and is shown in Figure S2 of the supplementary material.<sup>26</sup> The geometry of TMA at this point of near degeneracy is reminiscent of Tw-B “bending” conical intersection geometries of allene, 1,2-BD, and TMA.

## D. Simulation of excited-state dynamics

### 1. Allene

The evolution of the time-dependent adiabatic state populations, following vertical excitation to the  $S_1$  state of allene, is shown in Figure 7(a). Internal conversion to the ground electronic state on a femtosecond time scale was observed to occur. By fitting a single exponential function to the calculated  $S_1$  state populations, a time scale of 105 fs was determined for the lifetime of this state.

In order to elucidate information about the pathways to internal conversion which are operative in the  $S_1$  state of allene, we consider the locus of geometries at which the spawning

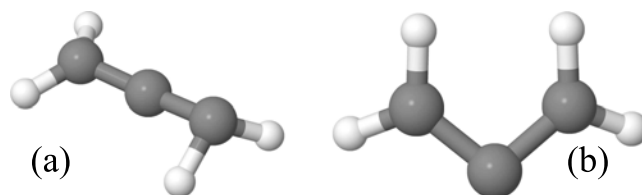


FIG. 6. Minimum energy conical intersection (CI) geometries between the  $S_0$  and  $S_1$  states for allene: (a) the Tw-Py CI and (b) the Tw-B CI. Analogous geometries for 1,2-BD, DMA, and TMA are given in Figure S2 of the supplementary material.<sup>26</sup>

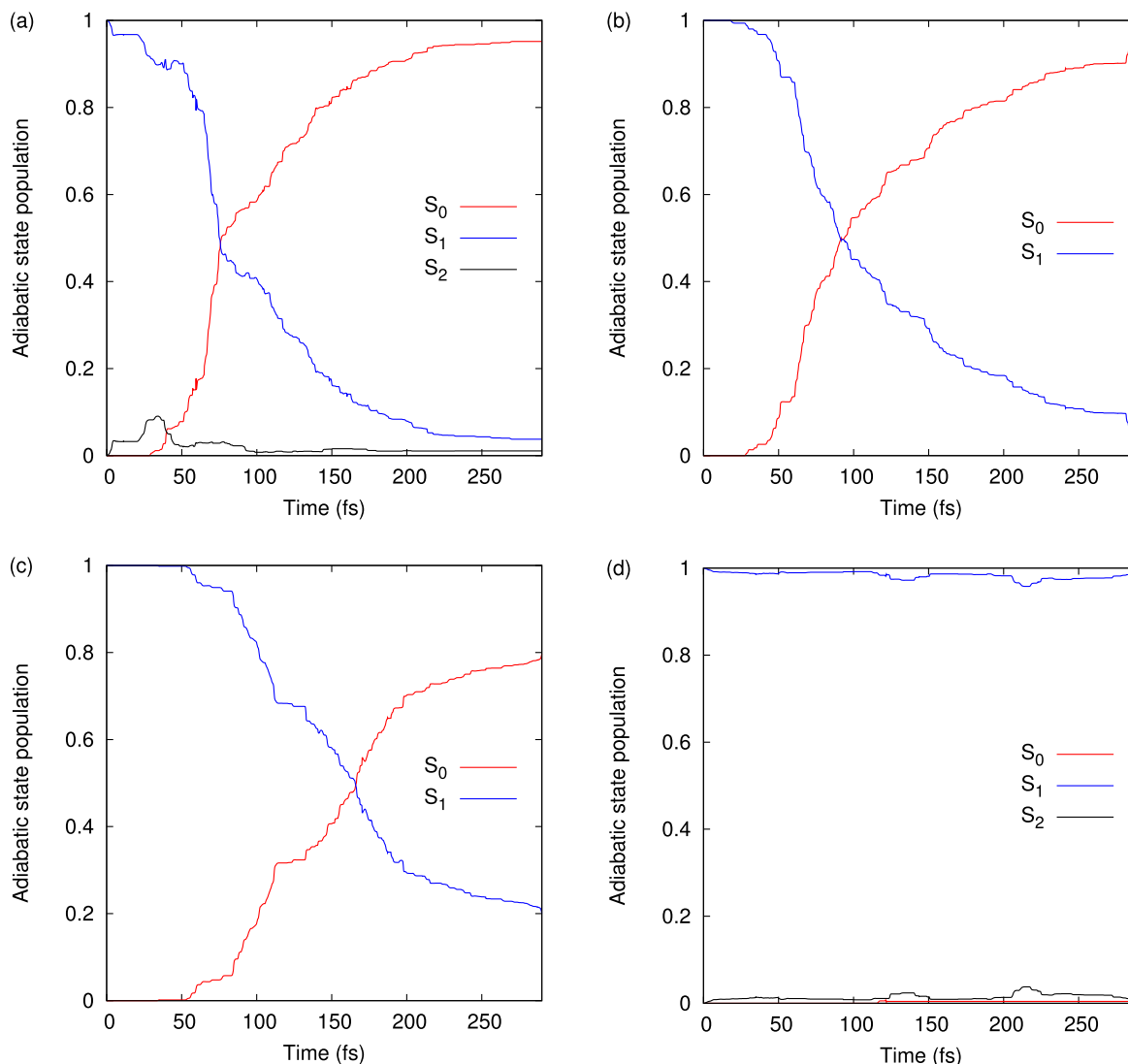


FIG. 7. Adiabatic state populations calculated using the AIMS trajectory method following vertical excitation to the  $S_1$  state for (a) allene, (b) 1,2-BD, (c) DMA, and (d) TMA.

of basis functions to the  $S_0$  state occurs, that is, geometries at which the coupling between the  $S_0$  and  $S_1$  states are large in magnitude. We found that the vast majority of spawn geometries involve large amplitude deformation along the twisting nuclear degree of freedom  $\psi$ , and, to a lesser extent, bending of the C–C–C backbone, corresponding to the nuclear degree of freedom  $\chi$ . We therefore postulate that internal conversion to the ground state is mediated predominantly by the Tw-Py and Tw-B conical intersections (illustrated in Figures 6(a) and 6(b)). In order to estimate the branching between these two conical intersections, we determined the minimum root mean square deviation of each spawn geometry from each conical intersection geometry subject to rotations and centre of mass translations using the so-called Kabsch algorithm.<sup>41</sup> We found that 37% of the spawn geometries map onto the Tw-B geometry, whilst 63% map onto the Tw-Py geometry. Thus, although both conical intersections play an important role in relaxation to the  $S_0$  state, internal conversion through Tw-Py intersection is dominant. This behavior may be partly explained by an analysis of the topography of the  $S_1$  PES in the space spanned by the twisting and bending

coordinates  $\psi$  and  $\chi$ , shown in Figure 8(a). At the FC point ( $\chi = 180^\circ$ ,  $\psi = 90^\circ$ ), the barriers to deformation along both degrees of freedom  $\chi$  and  $\psi$  are essentially zero, from which we may expect that large amplitude motion along either degrees of freedom could occur. However, with respect to the  $S_1$  PES, these two degrees of freedom are strongly coupled, a consequence of which is that once the local minimum at  $\psi = 0^\circ$  has been reached, there will exist a barrier to movement along  $\chi$ . Hence, the extent of deformation along the twisting coordinate  $\psi$  effectively modulates the propensity for movement along the bending coordinate  $\chi$ . That internal conversion to the ground state preferentially mediated by the Tw-Py conical intersection implies that initial large amplitude motion along the degree of freedom  $\psi$  occurs on a relatively fast time scale. This may be rationalized by reference to the  $S_1$  state projected mode imaginary frequencies corresponding to twisting and bending degrees of freedom at the FC point. At the MR-FOCI(4,4) level, the twisting and bending degrees of freedom are predicted to have projected mode frequencies of 2034 and 1231  $\text{cm}^{-1}$ , respectively. Hence, for the short time scale dynamics of allene, we may expect that large

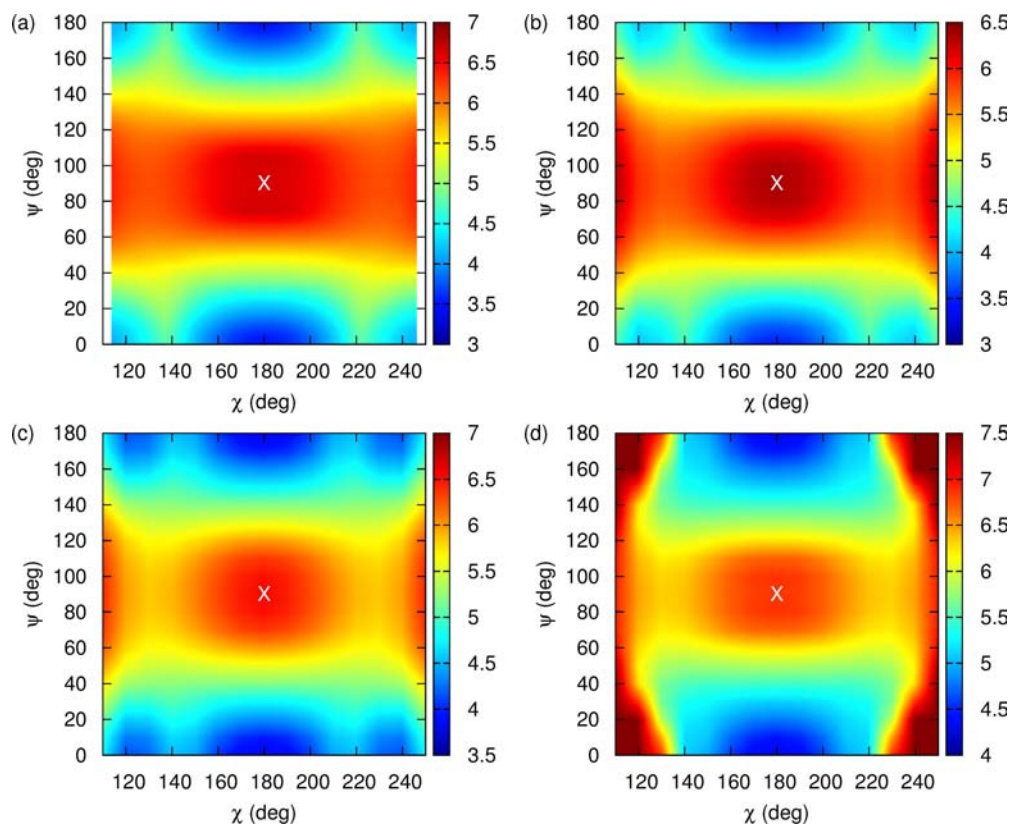


FIG. 8.  $S_1$  PES for (a) allene, (b) 1,2-BD, (c) DMA, and (d) TMA in the two-dimensional space spanned by the twisting coordinate  $\psi$  and the C–C–C bending coordinate  $\chi$ , as calculated at the MR-FOCI(4,4) level of theory. For each molecule, the white cross marks the location of the Franck-Condon point. As discussed in the text, it is the interplay of inertial and potential (steric) effects which governs the dynamics of these systems.

amplitude motion along the twisting degree of freedom  $\psi$  may occur more rapidly than motion along the bending degree of freedom  $\chi$ .

Corroboration of this picture is provided by the calculation of one-dimensional reduced nuclear densities  $\rho(s)$ ,

$$\rho(s) = \int |\Psi(\mathbf{R})|^2 \delta(f^{(s)}(\mathbf{R}) - s) d\mathbf{R}, \quad (8)$$

where  $s = \psi, \chi$  and  $f^{(s)}(\mathbf{R})$  denotes the function  $f^{(s)} : \mathbf{R} \rightarrow s$ . The reduced densities were evaluated using a Monte Carlo procedure, the details of which are described in Ref. 42. The one-dimensional reduced densities for the twisting coordinate  $\psi$  and bending coordinate  $\chi$ , calculated following excitation to the  $S_1$  state of allene, are shown in Figure 9(a). Frustration of the bending of the C–C–C backbone in the  $S_1$  state is found to occur, with a significant proportion of the  $S_1$  state population remaining trapped in the subspace for which the C–C–C backbone is approximately linear. Concomitantly, delocalization of the wavepacket along the twisting degree of freedom  $\psi$  occurs on an ultrafast time scale. Hence, support is given to the proposition that rapid twisting about the central allenic C–C–C unit effectively inhibits the comparatively slow bending of this moiety.

## 2. 1,2-butadiene

Shown in Figure 7(b) are the adiabatic state populations calculated following vertical excitation to the  $S_1$  state of

1,2-BD. The initially excited state is predicted to decay to the ground state on a time scale of 110 fs. Shown in Figure 8(b) is the  $S_1$  PES of 1,2-BD as a function of the twisting coordinate  $\psi$  and the bending coordinate  $\chi$ . The topography of this potential function is very similar to that for allene, with the barrier to displacement along the bending coordinate  $\chi$  being found to be increased significantly by movement along the twisting coordinate  $\psi$ . Accordingly, we may expect that internal conversion via the Tw-Py intersection will be dominant, as in the case of allene. Indeed, we found that 18% of the spawn geometries map onto the Tw-B geometry, whilst 82% map onto the Tw-Py geometry. This, interestingly, corresponds to an almost twofold decrease in the population passing through the Tw-B intersection as compared to allene. Such behaviour may be rationalized by reference to the ratio between the FC point projected mode frequencies of the twisting and bending modes in the  $S_1$  state, which (vide supra) we denote as  $\Gamma_\chi^\psi$ . For allene, we calculate  $\Gamma_\chi^\psi = 1.65$ , whilst for 1,2-BD,  $\Gamma_\chi^\psi = 2.00$ . Hence, given that the  $S_1$  PESs for both molecules are qualitatively similar in the space spanned by the bending and twisting degrees of freedom, we expect that the inhibition of the slower bending of the allenic C–C–C unit by the faster large amplitude motion along the twisting coordinate should be more effective for 1,2-BD than for allene. As such, the decrease in the population passing through the Tw-B intersection in 1,2-BD can be rationalized. For comparison, the calculated  $S_1$  state FC point projected mode frequencies corresponding to the twisting and bending modes for all four

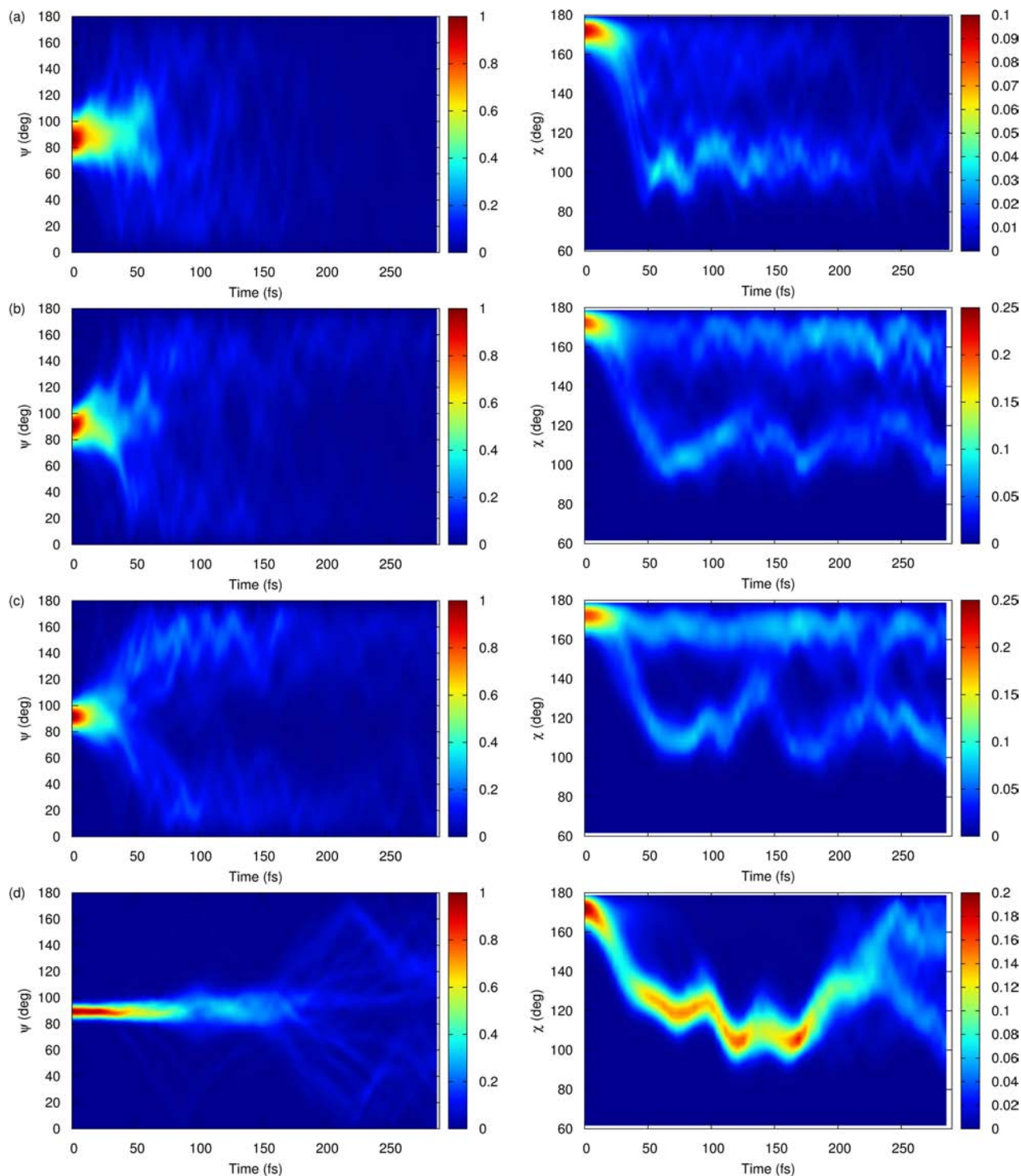


FIG. 9. Reduced densities for the twisting coordinate  $\psi$  (left-hand column) and C–C–C bending coordinate  $\chi$  (right-hand column) following excitation to the  $S_1$  state for (a) allene, (b) 1,2-BD, (c) DMA, and (d) TMA.

molecules considered here are given in Table II. For reference, the reduced densities for the twisting coordinate  $\psi$  and the bending coordinate  $\chi$  following excitation to the  $S_1$  state of 1,2-BD are shown in Figure 9(b).

### 3. DMA

Shown in Figure 7(c) are the adiabatic state populations for DMA calculated following vertical excitation to the  $S_1$

state. Ultrafast internal conversion to the ground electronic state is found to occur, with the lifetime of the  $S_1$  state in DMA being estimated to be  $\sim 160$  fs. The ratio  $\Gamma_{\chi}^{\psi}$  of the calculated FC point  $S_1$ -state twisting and bending projected mode frequencies for DMA is found to take a value of 1.96, which is to be compared to a value of 1.65 for allene. In analogy to 1,2-BD, from this increase in the value of  $\Gamma_{\chi}^{\psi}$ , we expect the population passing through the Tw-B geometry to be reduced relative to allene. However, we determined that

TABLE II.  $S_1(\pi\pi^*)$  state projected mode frequencies for allene, 1,2-BD, DMA, and TMA at the Franck-Condon point calculated at the MR-FOCI(4,4) level of theory.  $\omega_\psi$ : frequency for dihedral twisting about the allenic C–C–C unit.  $\omega_\chi$ : frequency for bending of the allenic C–C–C unit.  $\Gamma_\chi^\psi$ : ratio of  $\omega_\psi$  to  $\omega_\chi$ . All frequencies are given in units of  $\text{cm}^{-1}$ .

	Allene	1,2-BD	DMA	TMA
$\omega_\psi$	2034	1025	1605	716
$\omega_\chi$	1231	513	817	683
$\Gamma_\chi^\psi$	1.65	2.00	1.96	1.05

63% of spawn geometries mapped onto the Tw-Py intersection geometry, with the remaining 37% mapping onto the Tw-B geometry, which is to be compared the values of 67% and 33% for allene. It seems surprising that the propensity for internal conversion in DMA to proceed via the Tw-B intersection is not significantly decreased relative to allene, despite the significant increase in the value of  $\Gamma_\chi^\psi$ . However, this result may be rationalized by reference to the  $S_1$ -state PES of DMA as a function of the twisting and bending coordinates, shown in Figure 8(c). Perhaps unsurprisingly, both inertial and potential effects seem to play a role in the DMA dynamical branching pathways. We found that the height of the barrier to bending of the allenic C–C–C unit at quasi-planar geometries is diminished in DMA relative to allene. Hence, even though quasi-planarization of DMA is found to occur on an ultrafast time scale (as shown in Figure 9(c)), the resulting hindrance of large amplitude motion along the bending coordinate should be somewhat smaller for DMA than for allene. As such, an increase in the amount of population reaching the vicinity of the Tw-B conical intersection may be expected for DMA relative to allene, even though the ratio  $\Gamma_\chi^\psi$  is significantly increased.

#### 4. TMA

Shown in Figure 7(d) are the calculated adiabatic state populations following vertical excitation to the  $S_1$  state of TMA. Population is found to remain trapped in the initially excited state, with internal conversion to the ground electronic state being effectively hindered during the first 300 fs following excitation. This is in stark contrast to allene, 1,2-BD, and DMA, for which internal conversion to the ground state was predicted to occur on an ultrafast time scale. Explanation of this behavior is partly provided from a consideration of the calculated reduced densities for the dihedral degree of freedom  $\psi$  for TMA, as shown in Figure 9(d). Unlike in the cases of allene, 1,2-BD, and DMA, the wavepacket in the initially excited  $S_1$  state is found to remain localized about quasi-planar geometries for the first  $\sim 100$  fs, a consequence of a significant lowering of the FC point  $S_1$ -state projected mode frequency corresponding to the twisting degree of freedom upon complete methylation of the terminal allenic carbon atoms: in other words, it appears to be an inertial effect. As mentioned in Section IV C, no conical intersections between the  $S_0$  and  $S_1$  states could be found for TMA. However, a point of near degeneracy reminiscent of Tw-B conical intersection geometries of allene, 1,2-BD,

and DMA was found to exist. We thus postulate that large amplitude motion along the twisting degree of freedom  $\psi$  will be required for internal conversion to the ground state in TMA.

It appears that the inertial hindrance of torsional motion in TMA effectively inhibits internal conversion to the  $S_0$  state. Additionally, an increase in steric hindrance (a potential effect) brought about by the complete methylation of the terminal carbon atoms may also frustrate the passage of the wavepacket to the low-lying seams of intersection with the  $S_0$  state. In order to determine which of the inertial or potential (steric) effects are dominant in TMA, the FMS calculations for allene were re-run employing artificial hydrogen atoms of mass equal to that of the methyl group (15.03 a.u.). If the FMS calculations for this fictitious heavy hydrogen model system furnish similar results to the TMA calculations, then this is indicative that inertial effects are largely responsible for the hindrance of internal conversion to  $S_0$ . For the sake of brevity, the results are not reproduced here, but are shown in Figures S3-S5 of the supplementary material.<sup>26</sup> We found that the early time dynamics ( $t \lesssim 100$  fs) of the heavy hydrogen allene model are very similar to those of TMA, both in terms of the calculated adiabatic state populations and the calculated one-dimensional reduced densities for  $\psi$  and  $\chi$ . This strongly implies that the hindrance of internal conversion to the  $S_0$  state in TMA is indeed partially due to inertial effects introduced by the complete methylation of the terminal carbon atoms. However, beyond  $\sim 100$  fs, when delocalization along the twisting coordinate  $\psi$  occurs, rapid internal conversion to the  $S_0$  state is found to occur in the heavy hydrogen allene model. This discrepancy suggests that the increased steric hindrance introduced by the terminal methyl groups in TMA impedes passage of the wavepacket to the intersection seams between the  $S_1$  and  $S_0$  states. As such, we conclude that at longer time delays ( $t \gtrsim 100$  fs), steric hindrance effects are primarily responsible for the trapping of the wavepacket in the  $S_1$  state.

Another consequence of the inertial hindrance of twisting about the allenic C–C–C unit in TMA is that larger amplitude motion along the bending coordinate  $\chi$  was found to occur. As shown in Figure 9(d), unhindered large amplitude motion along the bending angle  $\chi$  is found to occur, enabled by the initial localization of the wavepacket around quasi-planar geometries. This is in contrast to allene, 1,2-BD, and DMA, for which a significant proportion of the wavepacket in the  $S_1$  state was found to remain localized around  $\chi \sim 180^\circ$ . As discussed in Section IV D 2, this behavior is explained by the strong coupling of the degrees of freedom  $\chi$  and  $\psi$ : barriers to motion along  $\chi$  are introduced by large amplitude motion along  $\psi$ . We specifically note that the magnitudes of these barriers may be modified by potential (steric) effects.

#### E. Calculated time-resolved photoelectron spectra

Shown in Figure 10 is the calculated TRPES corresponding to excitation to the  $S_1$  states of allene, 1,2-BD, DMA, and TMA. To aid the comparison of the calculated TRPES with their experimental counterparts, we show in Figure 11 a comparison of the calculated and experimental photoelectron

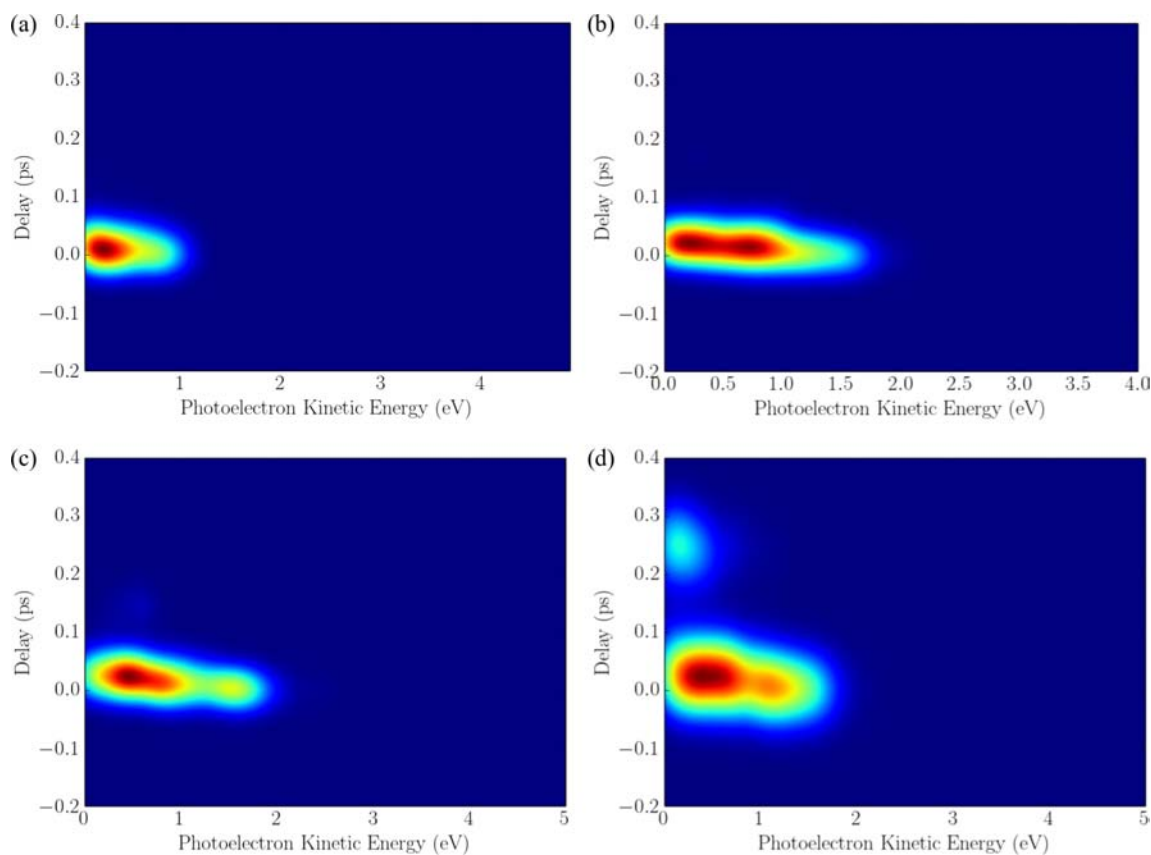


FIG. 10. TRPES calculated using AIMS trajectory data for (a) allene, (b) 1,2-BD, (c) DMA and (d) TMA following excitation to the  $S_1$  state.

intensities at single photoelectron kinetic energies of interest for 1,2-BD, DMA, and TMA. For 1,2-BD and DMA, we choose to focus the photoelectron kinetic energies around which the maxima of the experimental TRPES are centred: 0.36 eV and 0.46 eV for 1,2-BD and DMA, respectively. For TMA, we focus on a photoelectron kinetic energy of 0.22 eV, an energy at which the experimental TRPES exhibits non-negligible intensity for long time delays. For 1,2-BD and DMA, the agreement between the experimental and calculated photoelectron intensities is in general good. However, the decay of photoelectron signal in the experimental spectrum is found to occur on a slightly slower time scale in both cases. For TMA, the calculated TRPES captures the persistence of a significant photoelectron intensity in the low-energy region of the experimental spectrum for long time delays. However, relative to the experimental TRPES, the intensity in this low-energy part of the calculated TRPES is too low between time delays of around 100 and 200 fs. We attribute this discrepancy to the fact that, at longer time delays, the wavefunction is found to occupy regions of configuration space for which the ionization potential of the populated  $S_1$  state is very close to the photon energy of the probe laser pulse. In other words, certain configurations may be just outside the “ionization window” of the probe laser, leading to an apparent reduction in signal intensity. Highly accurate calculated vertical ionization energies may be required for the description of such near-threshold ionization processes, which are not compatible with the criterion of computational tractability required for direct dynamics calculation. Overall,

however, we note that the calculated and experimental TRPES exhibit the same qualitative features, namely, the persistence of the population in regions of nuclear configuration space where the  $S_1$  vertical ionization potential is very close to the energy of the probe photon. This agreement therefore validates the AIMS calculations underlying the calculated TRPES spectra.

For allene, 1,2-BD, and DMA, the calculated TRPES is found to decay on time scales of less than 100 fs. We note that in all cases, this time scale is significantly shorter than the rate of internal conversion to the ground electronic state. We thus determine that the major factor involved in the decay of the photoelectron signal is not the re-population of the  $S_0$  state but rather the passage of the wavepacket to low-energy regions on the  $S_1$  PES for which the instantaneous vertical ionization potential is raised above the photon energy of the probe laser pulse—the so-called ionization window. In particular, with reference to the results of the AIMS calculations discussed in Section IV D, it seems likely that large amplitude motion along the twisting coordinate  $\psi$  is primarily responsible for the ultrafast decay seen in the photoelectron signals for allene, 1,2-BD, and DMA. In contrast, the calculated TRPES for TMA is found to contain significant non-zero amplitude at low photoelectron energies for times extending to 300 fs, in broad agreement with the experimental TRPES. This is rationalized by the observed inertial hindrance of motion along the twisting degree of freedom  $\psi$  in TMA, leading to an increase in the time taken for the system to pass out of the ionization window.

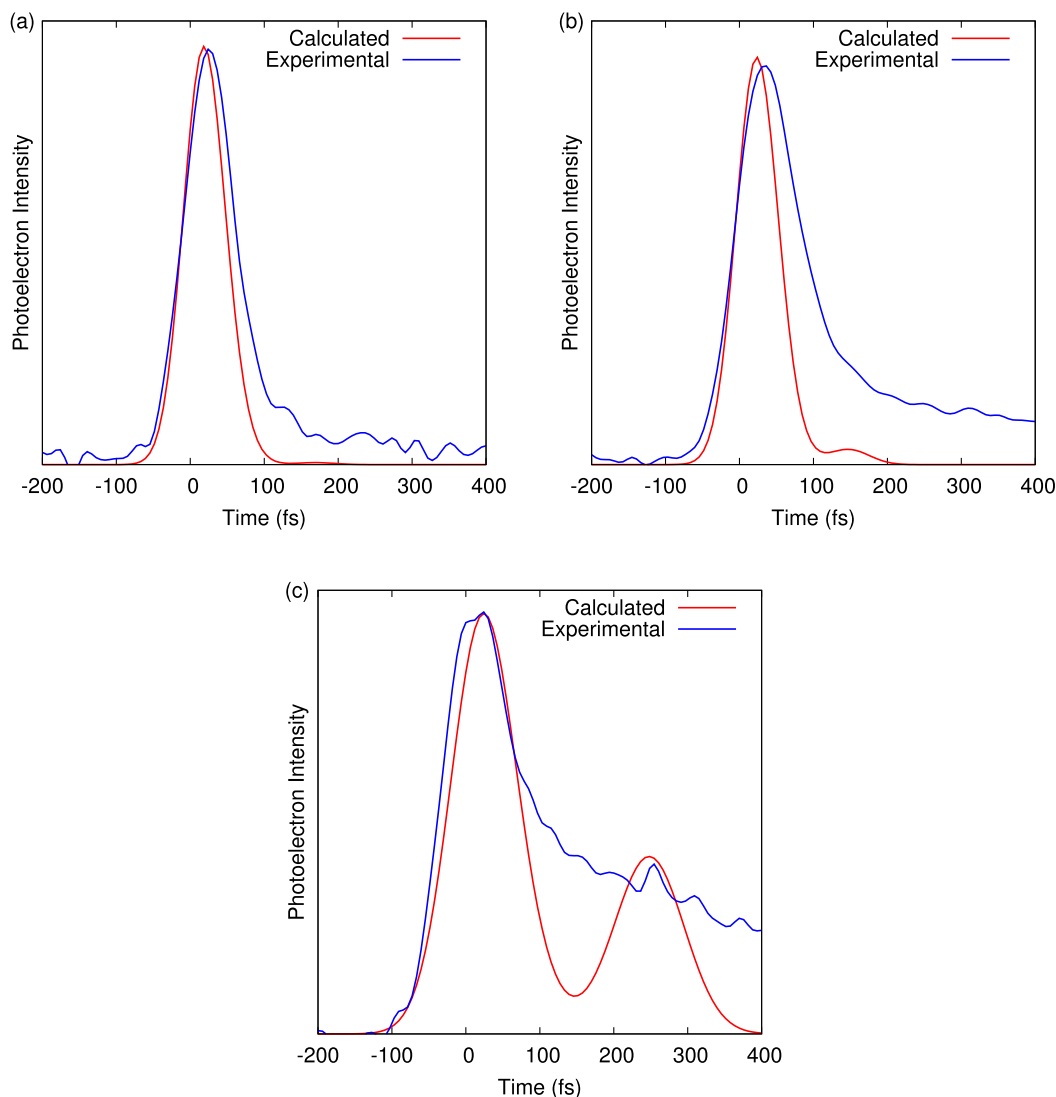


FIG. 11. Comparison of cuts along the experimental and calculated TRPES for single photoelectron kinetic energies  $E_{el}$  of interest. (a) 1,2-BD ( $E_{el} = 0.36$  eV), (b) DMA ( $E_{el} = 0.46$  eV), and (c) TMA ( $E_{el} = 0.22$  eV).

## V. DISCUSSION

For allene, 1,2-BD, DMA, and TMA, we expect that excitation at 200 nm results in population of the bright  $S_1(\pi\pi^*)$  state. TRPES for 1,2-BD, DMA, and TMA calculated from AIMS simulations corresponding to excitation to the  $S_1(\pi\pi^*)$  state are found to be in good agreement with the experimental TRPES for all three molecules, giving strong support to this assumption. For all molecules, the decay of the calculated TRPES signal is found to occur on a time scale faster than that for internal conversion to the  $S_0$  state. Hence, we reach the conclusion that the decay of the TRPES signal in each case is mediated primarily by the ultrafast passage of the wavepacket out of the ionization window in the initially excited  $S_1$  state. In turn, the increase in the ionization potential is found to be mediated mainly by large amplitude motion corresponding to twisting about the allenic C–C–C axis and/or bending of this unit.

For allene, 1,2-BD, and DMA, efficient internal conversion to the  $S_0$  state was found to be mediated by two common classes of conical intersection, which we termed the

Tw-Py (“twisting”) and Tw-B (“bending”) intersections (see Figure 6). The branching ratio for internal conversion through the Tw-Py and Tw-B intersections depended sensitively on the interplay between (i) inertial effects that determine the relative time scales for motion along the twisting and bending degrees of freedom  $\psi$  and  $\chi$ , respectively, and (ii) the degree and nature of the coupling of these nuclear coordinates on the  $S_1$  potential. In a chemically intuitive sense, we expect that, in these allenic systems, twisting leads to increased overlap of the  $\pi$ -electron system, thereby stiffening the backbone and inhibiting bending. For allene, 1,2-BD, and DMA, the ratio  $\Gamma_\chi^\psi$  between the FC point  $S_1$ -state projected mode frequencies corresponding to the twisting and bending motion is significantly greater than unity. Hence, for these systems, we expect large amplitude motion along the twisting degree of freedom to occur on a time scale faster than large amplitude motion along the bending degree of freedom. In turn, this hinders the bending of the allenic C–C–C unit, the extent of which is dependent upon both the magnitude of  $\Gamma_\chi^\psi$  and the size of the potential barrier to bending at quasi-planar geometries. For TMA, the methylation of both

terminal carbon atoms results in a strong decrease of the kinetic energy conjugate to the twisting degree of freedom. Consequently, the time scale for twisting about the allenic C–C–C axis is significantly increased relative to that for allene, 1,2-BD, and DMA. The inertial slowing of the twisting dynamics prevents the stiffening of the carbon backbone on time scales fast compared to bending. A result of this is that motion along the bending coordinate may now occur in an essentially uninhibited manner, leading to a trapping of the wavepacket in a subspace for which the ionization potential is raised to a value close to the photon energy of the probe laser pulse (the edge of the ionization window, meaning very low energy electrons). Additionally, steric effects resulting from the methylation of the terminal carbon atoms in TMA are predicted to result in a frustration of the passage of the wavepacket to the seams of intersection between the  $S_1$  and  $S_0$  states. This trapping of the excited state wavepacket manifests itself in the delayed rise of a weak, low very kinetic energy feature in the TRPES of TMA. This yield of low kinetic energy photoelectrons persists for some hundreds of fs (*vide infra*), whereupon the comparatively slow twisting about the allenic C–C–C unit drives the system fully out of the ionization window.

The results of the AIMS simulations discussed above are supported by the agreement of the calculated TRPES for 1,2-BD, DMA, and TMA with their experimental counterparts. For all systems, the decay of the experimental TRPES signal is characterized by both short and long time constants: 30 fs and 1.8 ps for 1,2-BD, 52 fs, and 3.5 ps for DMA, and 23 fs, 306 fs and 18 ps for TMA. We assign the short time constants in all cases to large amplitude motion taking the system out of the ionization window on an ultrafast time scale. The long time constants in each case are assigned to the decay of those parts of the wavepacket that remain trapped in the proximity of the FC zone.

For TMA, coherent oscillations with a period of  $\sim 50$  fs are observed in the low-energy region of the experimental TRPES, persisting for about 300 fs. This corresponds to a vibrational frequency of  $\sim 670$   $\text{cm}^{-1}$ , which matches the calculated FC point  $S_1$ -state projected mode frequency of the C–C–C bending coordinate ( $683$   $\text{cm}^{-1}$ ) reasonably well. It is thus tempting to assign these low-energy oscillations to bending of the allenic C–C–C unit in the  $S_1$  state. This interpretation is further supported by the results of the AIMS calculations for TMA. These predict both a trapping of the wavepacket in the  $S_1$  state and coherent oscillatory motion along the bending coordinate  $\chi$  for the first 200 fs (see the reduced density plot in Figure 9(d)). This behaviour may be explained with reference to strong coupling between the bending and twisting coordinates,  $\chi$  and  $\psi$ , as manifested in the  $S_1$  state PES (shown in Figure 8(d)). As discussed above, large amplitude motion along the twisting degree of freedom  $\psi$  inhibits deformation along the bending degree of freedom  $\chi$ , inducing an increased barrier to the latter in the  $S_1$  state PES. However, as a result of inertial effects due to complete methylation in TMA, the time scale for twisting becomes relatively long, allowing the wavepacket to sample regions of nuclear configuration space proximate to the local minima around bending angles of  $\chi = 130^\circ$  and  $230^\circ$ . The

relatively long (few hundred fs) time scale of the ensuing oscillations in the bending coordinate may be rationalized if this coordinate remains coupled to the slower twisting degree of freedom, but relatively isolated from the remaining subset of vibrations having similar or higher frequencies. From the AIMS simulations of TMA, the reduced densities shown in Figure 9(d) reveal that the disappearance of coherent oscillations in the bending coordinate coincides with the onset of large amplitude motion along the twisting degree of freedom. Again, this behaviour may be rationalized with reference to the topography of the  $S_1$  state PES as a function of these two nuclear degrees of freedom, as illustrated in Figure 8(d). Starting from the local minima at bending angles of  $\chi = 130^\circ$  and  $230^\circ$ , displacement along the twisting degree of freedom  $\psi$  results in the formation of negative gradients in the direction of  $\chi = 180^\circ$ . The effect of this is to funnel the wavepacket back to a subspace for which the allenic C–C–C unit is approximately linear. This may be seen in the reduced density plots in Figure 9(d). At around 150 fs, the wavepacket finally begins to delocalize along the twisting degree of freedom  $\psi$ , with some of the population evolving to values of  $\psi$  for which the system is quasi-planar. Some population, however, also remains around the initial value of  $\psi$ . This is seen as a bifurcation in the reduced density along the bending coordinate  $\chi$ , with delocalisation along  $\psi$  driving a partial return to a quasi-linear arrangement of the allenic C–C–C unit.

Finally, we recall that the experimental TRPES for 1,2-BD, DMA, and TMA all exhibited “sweeps” of the photoelectron signal towards lower kinetic energies at longer times, implying the existence of large amplitude motion in the initially excited state of each molecule. This is fully consistent with the results of the AIMS calculation, which predict large amplitude motion to occur in the  $S_1$  state along both the twisting  $\psi$  and bending  $\chi$  degrees of freedom.

## VI. CONCLUSIONS

Identifying the conical intersections connecting a given electronic state to its neighbouring states is a key to understanding ultrafast excited state relaxation dynamics in a molecular system. It may be thought that the knowledge of the barrier along the minimum energy pathway connecting the FC region to a point of conical intersection suffices to determine the importance of that intersection in the excited state relaxation dynamics. We emphasize, however, that excited state relaxation is inherently dynamical in nature and a static investigation based solely on the identification of critical points on the PES is very unlikely to be sufficient. Rather, when two or more conical intersections are, in energetic terms, equally accessible to the excited state wavepacket, the relative time scales for motion along the nuclear degrees of freedom connecting the FC region to the intersection seams of interest become critical. Additionally, the possibility of strong coupling of these nuclear coordinates can also have a profound effect upon the observed relaxation dynamics. Both of these effects are exemplified in the dynamics of allene and its methylated analogues following excitation to

their  $S_1(\pi\pi^*)$  states. Importantly, a purely static study of the potential barriers along minimum energy pathways would fail to explain the dynamics observed in these molecules.

In the case of allene, 1,2-BD, and DMA, internal conversion from the  $S_1(\pi\pi^*)$  state to the ground state is found to be predominantly facilitated by two types of conical intersection, the geometries which we label as Tw-Py and Tw-B. Both involve twisting about the allenic C–C–C axis, but with this unit being linear for the Tw-Py geometries and bent for the Tw-B geometries. Although the pathways to both sets of geometries from the FC point are essentially barrierless, internal conversion through the Tw-Py intersections is found to dominate in all cases. This is partly attributable to motion along the higher imaginary frequency twisting coordinate occurring on a time scale faster than motion along the lower frequency bending coordinate. Importantly, the high degree of correlation between these two degrees of freedom leads to an increase in the barrier to bending upon quasi-planarization, contributing further to the dominance of internal conversion via the Tw-Py intersections. In our chemically intuitive picture, large amplitude twisting in the excited state leads to an increase in the delocalization of the  $\pi$  orbital system, thereby stiffening the C–C–C unit. For TMA, the effect of complete methylation of the terminal carbon atoms is, as expected by the increased inertia, to decrease the kinetic energy conjugate to the twisting coordinate, resulting in an increase in the time taken for quasi-planarization to occur. Consequently, bending of the allenic C–C–C unit is uninhibited, trapping the excited state wavepacket in a low-energy subspace just within the ionization window for around 300 fs.

It is often remarked that conical intersections are the “transition states” of the excited state. This may tempt one to consider the development of a “transition state”-like statistical or reduced phase space theory for dynamics at conical intersections. However, based on the reasoning above, we doubt that a microcanonical “transition state” type of unimolecular decay theory will apply extensively for such dynamics. Rather, as the results presented here strongly suggest, we anticipate that a dynamical approach to excited state processes at conical intersections will need to be fully developed.

## ACKNOWLEDGMENTS

Y.W. acknowledges the Young Visiting Scholar Programme of Wuhan Institute of Physics and Mathematics, Chinese Academy of Sciences, and National Natural Science Foundation of China under Grant No. 21173256. A.S. thanks NSERC, via its Discovery Grant program, and the Canada Research Chairs for financial support. M.S. thanks NSERC for financial support.

<sup>1</sup>S. H. Lee, K. C. Tang, I. C. Chen, M. Schmitt, J. P. Shaffer, T. Schultz, J. G. Underwood, M. Z. Zgierski, and A. Stolow, *J. Phys. Chem. A* **106**, 8979 (2002).

<sup>2</sup>G. Wu, A. E. Boguslavskiy, O. Schalk, M. S. Schuurman, and A. Stolow, *J. Chem. Phys.* **135**, 164309 (2011).

<sup>3</sup>A. M. Lee, J. D. Coe, S. Ullrich, M. L. Ho, S. J. Lee, B. M. Cheng, M. Z. Zgierski, I. C. Chen, T. J. Martinez, and A. Stolow, *J. Phys. Chem. A* **111**, 11948 (2007).

<sup>4</sup>O. Schalk, A. E. Boguslavskiy, and A. Stolow, *J. Phys. Chem. A* **114**, 4058 (2010).

<sup>5</sup>O. Schalk, A. E. Boguslavskiy, A. Stolow, and M. S. Schuurman, *J. Am. Chem. Soc.* **133**, 16451 (2011).

<sup>6</sup>T. J. A. Wolf, T. S. Kuhlman, O. Schalk, T. J. Martínez, K. B. Møller, A. Stolow, and A.-N. Unterreiner, *Phys. Chem. Chem. Phys.* **16**, 11770 (2014).

<sup>7</sup>O. Schalk, A. E. Boguslavskiy, M. S. Schuurman, R. Y. Brogaard, A. N. Unterreiner, A. Wrona-Piotrowicz, N. H. Werstiuk, and A. Stolow, *J. Phys. Chem. A* **117**, 10239 (2013).

<sup>8</sup>T. Shimizu, in *CRC Handbook of Organic Photochemistry and Photobiology*, edited by W. M. Horspool and F. Lenci (CRC Press, Boca Raton, FL, 2004).

<sup>9</sup>W. Sun, K. Yokoyama, J. C. Robinson, A. G. Suits, and D. M. Neumark, *J. Chem. Phys.* **110**, 4363 (1999).

<sup>10</sup>R. H. Qadiri, E. J. Feltham, N. H. Nahler, R. P. Garcia, and M. N. R. Ashfold, *J. Chem. Phys.* **119**, 12842 (2003).

<sup>11</sup>A. Fahr and A. H. Laufer, *J. Phys. Chem. A* **109**, 2534 (2005).

<sup>12</sup>J. C. Robinson, N. E. Sveum, S. J. Goncher, and D. M. Neumark, *Mol. Phys.* **103**, 1765 (2005).

<sup>13</sup>W. M. Jackson, A. M. Mebel, S. H. Lin, and Y. T. Lee, *J. Phys. Chem. A* **101**, 6638 (1997).

<sup>14</sup>A. M. Mebel, W. M. Jackson, A. H. H. Chang, and S. H. Lin, *J. Am. Chem. Soc.* **120**, 5751 (1998).

<sup>15</sup>J. C. Robinson, W. Sun, S. A. Harris, F. Qi, and D. M. Neumark, *J. Chem. Phys.* **115**, 8359 (2001).

<sup>16</sup>H.-Y. Lee, V. V. Kislov, S.-H. Lin, A. M. Mebel, and D. M. Neumark, *Chem. - Eur. J.* **9**, 726 (2003).

<sup>17</sup>A. Hanf, H.-R. Volpp, P. Sharma, J. P. Mittal, and R. K. Vatsa, *J. Chem. Phys.* **133**, 024308 (2010).

<sup>18</sup>Z. Diaz and R. D. Doepker, *J. Phys. Chem.* **81**, 1442 (1977).

<sup>19</sup>X. Mu, I.-C. Lu, S.-H. Lee, X. Wang, and X. Yang, *J. Chem. Phys.* **121**, 4684 (2004).

<sup>20</sup>R. Iikubo, T. Fujiwara, T. Sekikawa, Y. Harabuchi, S. Satoh, T. Taketsugu, and Y. Kayanuma, *J. Phys. Chem. Lett.* **6**, 2463 (2015).

<sup>21</sup>A. Stolow, A. E. Bragg, and D. M. Neumark, *Chem. Rev.* **104**, 1719 (2004).

<sup>22</sup>A. Stolow and J. G. Underwood, *Adv. Chem. Phys.* **139**, 497 (2008).

<sup>23</sup>M. S. Schuurman and A. Stolow, in *Conical Intersections: Theory, Computation and Experiment* (World Scientific Publishing, 2011), Vol. 17, Chap. 16, p. 633.

<sup>24</sup>S. Lochbrunner, J. J. Larsen, J. P. Shaffer, M. Schmitt, T. Schultz, J. G. Underwood, and A. Stolow, *J. Electron Spectrosc. Relat. Phenom.* **112**, 183 (2000).

<sup>25</sup>C. Homann, N. Krebs, and E. Riedle, *Appl. Phys. B* **104**, 783 (2011).

<sup>26</sup>See supplementary material at <http://dx.doi.org/10.1063/1.4938561> for a description of the calculation of relative photoionization probabilities, spectra and autocorrelation traces, the pump and probe pulses, calculated minimum energy conical intersection geometries, and the results of the AIMS calculations for the heavy hydrogen atom allene model.

<sup>27</sup>G. W. Bethke, *J. Chem. Phys.* **31**, 662 (1959).

<sup>28</sup>G. K. Jarvis, M. Evans, C. Y. Ng, and K. Mitsuke, *J. Chem. Phys.* **111**, 3058 (1999).

<sup>29</sup>M. Ben-Nun and T. J. Martínez, *Adv. Chem. Phys.* **121**, 439 (2002).

<sup>30</sup>H. R. Hudcock, B. G. Levine, A. L. Thompson, H. Satzger, D. Townsend, N. Gador, S. Ulrich, A. Stolow, and T. J. Martínez, *J. Chem. Phys. A* **111**, 8500 (2007).

<sup>31</sup>H. R. Hudcock and T. J. Martínez, *Chem. Phys. Chem.* **9**, 2486 (2008).

<sup>32</sup>A. L. Thompson and T. J. Martínez, *Faraday Discuss.* **150**, 293 (2011).

<sup>33</sup>H. Tao, T. K. Allison, T. W. Wright, A. M. Stooke, C. Khurmi, J. van Tilborg, Y. Liu, R. W. Falcone, A. Belkacem, and T. J. Martínez, *J. Chem. Phys.* **134**, 244306 (2011).

<sup>34</sup>T. Mori, W. J. Glover, M. S. Schuurman, and T. J. Martínez, *J. Phys. Chem. A* **116**, 2808 (2012).

<sup>35</sup>T. S. Kuhlman, W. J. Glover, T. Mori, K. B. Møller, and T. J. Martínez, *Faraday Discuss.* **157**, 193 (2012).

<sup>36</sup>M. Spanner, S. Patchkovskii, C. Zhou, S. Matsika, M. Kotur, and T. C. Weinacht, *Phys. Rev. A* **86**, 053406 (2012).

<sup>37</sup>H. Lischka, R. Shepard, I. Shavitt, R. M. Pitzer, M. Dallos, T. Miller, P. G. Szalay, F. B. Brown, R. Ahlrichs, H. J. Bhm, A. Chang, D. C. Comeau, R. Gdanitz, H. Dachsels, C. Ehrhardt, M. Ernzerhof, P. Hchtl, S. Irlle, G. Kedziora, T. Kovar, V. Parasuk, M. J. M. Pepper, P. Scharf, H. Schiffer, M. Schindler, M. Schler, M. Seth, E. A. Stahlberg, J.-G. Zhao, S. Yabushita, Z. Zhang, M. Barbatti, S. Matsika, M. Schuurman, D. R. Yarkony, S. R. Brozell, E. V. Beck, J.-P. Blaudeau, M. Ruckentbauer, B. Sellner, F. Plassner, and J. J. Szycyzak, an *ab initio* electronic structure program, release 7.0, Columbus, 2015.

- <sup>38</sup>TURBOMOLE V6.1 2009, a development of University of Karlsruhe and Forschungszentrum Karlsruhe GmbH, 1989-2007, TURBOMOLE GmbH, 2007, available from <http://www.turbomole.com>.
- <sup>39</sup>CFOUR, a quantum chemical program package written by J. F. Stanton, J. Gauss, M. E. Harding, P. G. Szalay with contributions from A. A. Auer, R. J. Bartlett, U. Benedikt, C. Berger, D. E. Bernholdt, Y. J. Bomble, L. Cheng, O. Christiansen, M. Heckert, O. Heun, C. Huber, T.-C. Jagau, D. Jonsson, J. Jusélius, K. Klein, W.J. Lauderdale, D.A. Matthews, T. Metzroth, L. A. Mück, D. P. O'Neill, D. R. Price, E. Prochnow, C. Puzzarini, K. Ruud, F. Schiffmann, W. Schwalbach, C. Simmons, S. Stopkowicz, A. Tajti, J. Vázquez, F. Wang, J. D. Watts and the integral packages MOLECULE (J. Almlöf and P. R. Taylor), PROPS (P. R. Taylor), ABACUS (T. Helgaker, H. J. Aa. Jensen, P. Jørgensen, and J. Olsen), and ECP routines by A. V. Mitin and C. van Wüllen. For the current version, see <http://www.cfour.de>.
- <sup>40</sup>O. Schalk, M. S. Schuurman, G. Wu, P. Lang, M. Mucke, R. Feifel, and A. Stolow, *J. Phys. Chem. A* **118**, 2279 (2014).
- <sup>41</sup>W. Kabsch, *Acta Crystallogr.* **32**, 922 (1976).
- <sup>42</sup>J. D. Coe, B. G. Levine, and T. J. Martínez, *J. Phys. Chem. A* **111**, 11302 (2007).
- <sup>43</sup>F. Brogli, J. K. Crandall, E. Heilbronner, E. Kloster-Jensen, and S. A. Sojka, *J. Electron Spectrosc.* **2**, 455 (1973).